AGU PUBLICATIONS

JGR

Journal of Geophysical Research: Atmospheres

RESEARCH ARTICLE
10.1002/2017JD027903

Key Points:
- Ground validation shows that four surface net radiation products have similar accuracies but considerable spatial and temporal differences
- The negative global anomaly of the CERES R_n product for the period from 2001 to 2008 is spurious due to different input data versions
- Ground validation does not always reveal all quality issues in time series products, but temporal analysis can serve as complementary tool

Correspondence to:
S. Liang,
sliang@umd.edu

Citation:
Jia, A., Liang, S., Jiang, B., Zhang, X., & Wang, G. (2018). Comprehensive assessment of global surface net radiation products and uncertainty analysis. *Journal of Geophysical Research: Atmospheres*, *123*, 1970–1989. https://doi.org/10.1002/2017JD027903

Received 20 OCT 2017
Accepted 28 JAN 2018
Accepted article online 6 FEB 2018
Published online 18 FEB 2018

Comprehensive Assessment of Global Surface Net Radiation Products and Uncertainty Analysis

Aolin Jia[1], Shunlin Liang[2], Bo Jiang[1], Xiaotong Zhang[1], and Guoxin Wang[1]

[1]State Key Laboratory of Remote Sensing Science, Faculty of Geographical Science, Beijing Normal University, Beijing, China, [2]Department of Geographical Sciences, University of Maryland, College Park, MD, USA

Abstract Earth surface net radiation (R_n) characterizes the surface radiation budget and plays a critical role in ecological, biogeochemical, and hydrological processes. The R_n products from remote sensing and reanalysis have not been validated comprehensively. In this study, four R_n products (Clouds and the Earth's Radiant Energy System [CERES], ERA-Interim, Modern-Era Retrospective analysis for Research and Applications version 2, and Japanese 55-year Reanalysis) were validated using global ground measurements on monthly (255 sites) and annual (172 sites) timescales. These products have similar accuracies, with average root-mean-square error (RMSE) ranges of 5.35 W m^{-2} (monthly) and 2.30 W m^{-2} (annually). However, varying accuracies and systemic biases exist across different climatic zones. The annual land R_n intercomparison illustrates that large uncertainty exists over polar regions and deserts. A significantly negative annual anomaly in the CERES product for the 2001–2008 period is identified when examining annual R_n anomalies over the global land surface. Detailed uncertainty analysis indicates that the global CERES R_n anomaly is mainly due to different versions of input data such as aerosol optical thickness and atmospheric profiles (in 2006 and 2008) and cloud properties (in 2002). This work demonstrates that temporal analysis provides powerful quality control for global time series satellite products when the validation using ground measurements fails to capture potential issues.

1. Introduction

Earth surface net radiation (R_n), which characterizes the surface radiation budget, represents the balance between total incoming radiation from the atmosphere and upward-reflected shortwave radiation and emitted longwave radiation from different surfaces (Liang, 2004). Mathematically, R_n can be expressed as

$$R_n = R_n^s + R_n^l \tag{1}$$

$$R_n^s = (1-\alpha)R_d^s \tag{2}$$

$$R_n^l = R_d^l - R_u^l, \tag{3}$$

where R_n^s is the shortwave net radiation (W m^{-2}), R_n^l is the longwave net radiation (W m^{-2}), α is the shortwave broadband albedo, R_d^s is the downward shortwave radiation (W m^{-2}), and R_d^l and R_u^l are the downward longwave radiation (W m^{-2}) and upward longwave radiation (W m^{-2}), respectively.

The surface R_n constitutes the available radiative energy and can be transformed into latent flux, heat flux, and soil heat flux (Gupta et al., 1999). It plays a crucial role in ecological, biogeochemical, and hydrological processes (Liang et al., 2010; Ramanathan et al., 2001; Wild et al., 2013). Studying R_n is crucial for understanding land surface energy partitioning (Wilson et al., 2002), snowmelt (Sicart et al., 2004), and yield estimation (Zhang et al., 2001). Due to the heterogeneous distribution of the surface energy, R_n powers atmospheric circulation (Bretherton & Battisti, 2000; Cruz et al., 2005; Davies et al., 1987). Thus, accurate estimates of R_n are essential for terrestrial water, energy, and carbon research (Mercado et al., 2009; Wild et al., 2008; Yao et al., 2013).

Methods for calculating R_n include ground observations, reanalysis data sets, general circulation modelsimulations (Wild, 2008), and remote sensing retrievals (Liang et al., 2010). In situ ground observations have the highest accuracy but limited distribution and spatial representation and thus cannot satisfy many research demands on the global scale (Jia et al., 2016; Jiménez-Muñoz et al., 2012; Wild et al., 2015). Reanalysis data are derived by merging available observations with an atmospheric model (Decker et al., 2012), which may have uncertainties due to the modeled cloud information (Trenberth & Fasullo, 2010). The general circulation model simulations have coarse spatial resolution and less accuracy (Wild et al., 2013). Comparatively, remote

sensing retrievals have become one of the most vital methods for estimating R_n due to their spatial continuity and higher accuracy (Liang et al., 2010). All modeled and satellite R_n data sets need to be comprehensively validated.

Several remote sensing radiation products and reanalysis data sets have been validated using ground measurements on a regional scale (Wu & Fu, 2011; Xia et al., 2006). Gui et al. (2010) validated four satellite R_d^l products over North America and the Tibet Plateau. The authors reported that the International Satellite Cloud Climatology Project-Flux Data were overestimated, while the Clouds and the Earth's Radiant Energy System (CERES) data were underestimated. Pan et al. (2015) assessed the CERES and Surface Radiation Budget project data sets for China and found that 56% of the net radiation errors were due to shortwave radiation. Troy and Wood (2009) evaluated and compared two remote sensing radiation products and five reanalysis data sets for northern Eurasia, demonstrating that biases exist among different products. Although R_n products have been evaluated for different areas, the number of observations used in those studies is limited and regional validation work can neither characterize the overall accuracy of global R_n products nor provide strong evidence for the applicability of R_n data sets to different climate regions on large spatiotemporal scales.

Some land surface radiation data sets have been validated globally (Hinkelman et al., 2009; Jiang et al., 2015; Lin et al., 2008). Zhang et al. (2015) and Wang and Dickinson (2013) comprehensively reviewed and assessed R_d^s and R_d^l satellite products and corresponding reanalysis data sets. However, global R_n products still need to be comprehensively assessed globally. Kato et al. (2012) estimated the uncertainty of the CERES surface irradiance using multiple satellite sensors and limited ground measurements, demonstrating that the uncertainty of the global surface mean R_n is 12 W m^{-2}. They also utilized 24 global land sites to validate the CERES downward shortwave and longwave surface irradiances from 2000 to 2010, but the accuracy of R_n is still undetermined (Kato et al., 2013). Jia et al. (2016) validated the CERES Synoptic Radiative Fluxes (SYN) R_n products on a daily (340 sites) and monthly (260 sites) basis and reported that the daily validations have a mean bias error (MBE) of 3.43 W m^{-2}, RMSE of 33.56 W m^{-2}, and coefficient of determination (R^2) of 0.79. Similarly, the monthly validations have an MBE of 3.40 W m^{-2}, RMSE of 25.57 W m^{-2}, and R^2 of 0.84. Both prior global R_n validations addressed satellite products but did not include reanalyses, which are also valuable for the study of surface radiation budgets due to their lengthy temporal record and spatial continuity. Moreover, previous uncertainty analysis of surface R_n products did not involve input cloud information, which is a major error source (Jia et al., 2016; Pan et al., 2015). Most validations of the surface R_n focused on daily and monthly scales; however, annual assessment and validation for different climatic zones can be of greater value for climate research (Bye et al., 2011).

In this study, the global validation and intercomparison of four R_n products were implemented with uncertainty analysis of the CERES R_n. First, R_n measurements obtained from 15 worldwide ground networks (309 sites) from 2001 to 2013 were used to comprehensively validate the CERES Energy Balanced and Filled (EBAF) surface R_n product and three reanalysis R_n data sets, including the (1) ERA-Interim, (2) Modern-Era Retrospective analysis for Research and Applications version 2 (MERRA2), and (3) Japanese 55-year Reanalysis (JRA-55), on monthly and annual scales. Subsequently, spatial and longtime comparisons among these data sets were evaluated. Finally, the CERES R_n product has great potential for studying global surface energy budget variations. Thus, warranting particular focus on its variation authenticity and uncertainty, detailed uncertainty analysis of significant anomalies of the CERES R_n was carried out.

2. Data and Methodology

2.1. Data

2.1.1. Surface R_n Satellite Products

As one of the most advanced surface radiation satellite products, the CERES EBAF products (Kato et al., 2013) have great potential for studying the global surface energy budget variation and climate feedback, a topic necessitating assessment across large spatial scales. The EBAF Ed2.8 surface products are mainly driven by two sources: EBAF Top of Atmosphere (TOA) products in which computed TOA irradiances are constrained by CERES observations (Rose et al., 2013) and CERES SYN1deg-Month Ed3. The temperature and humidity profiles used in the radiative transfer model are driven by the Goddard Earth Observing System (GEOS-4

Table 1
Summary of Surface Radiation Products Used in This Study

Category	Name	Timespan	Spatial resolution	Temporal resolution
Satellite radiation products	CERES_EBAF-surface_Ed2.8	2001.01–2015.12	1° × 1°	Monthly
	CERES_EBAF-TOA_Ed2.8	2001.01–2015.12	1° × 1°	Monthly
	CERES_SYN1deg-Ed3A Surface Fluxes	2001.01–2015.12	1° × 1°	3-Hourly
	GLASS Surface Daytime R_n Product	2001.01–2008.12	0.05° × 0.05°	Daily
Reanalysis	ERA-Interim	1980.01–2015.12	0.75° × 0.75°	3-Hourly
	MERRA2	1980.01–2015.12	0.5° × 0.625°	Hourly
	JRA-55	1980.01–2013.12	0.563° × 0.563°	3-Hourly

and 5) Data Assimilation System reanalysis. The EBAF clear-sky data are separately adjusted to the monthly mean from CERES EBAF-TOA clear-sky "filled" observations. In this study, CERES EBAF monthly all-sky surface R_n products were validated and compared with other R_n reanalysis data sets. The EBAF-TOA products and clear-sky surface R_n data were used to detect annual variations in the global R_n cloud radiative forcing.

To check the CERES R_n anomaly, the 3-hourly CERES SYN R_n was bilinearly interpolated and averaged into daytime R_n and compared with the Global Land Surface Satellite (GLASS) daytime R_n product. The CERES SYN1deg Ed3A products provide CERES-observed temporally interpolated surface radiative fluxes and coincident Moderate Resolution Imaging Spectroradiometer (MODIS)-derived cloud and aerosol properties. The latter includes geostationary (GEO)-derived cloud properties and broadband fluxes that have been carefully normalized with CERES fluxes to maintain the CERES calibration (Doelling et al., 2013). Relevant MODIS aerosols and cloud parameters have also been released. The CERES SSF1deg Ed3A low-sky (700 mbar) cloud parameters (shown in Table 2), which are driven from Terra and Aqua, respectively, were compared with CERES SYN1deg low-sky cloud parameters to determine anomalous cloud R_n forcing in the uncertainty analysis.

As one of the newest global land net radiation products, the GLASS daytime R_n product (Jiang et al., 2016) was also used for comparison with the CERES daytime R_n to detect anomalous annual variations. The GLASS daytime R_n product converts shortwave radiation to all-wave net radiation using the Multivariate Adaptive Regression Splines model. Compared with the validation results from the CERES daytime R_n and other reanalysis products (MERRA and JRA-55), GLASS shows an average RMSE of 31.61 W m^{-2}, average bias of −17.59 W m^{-2}, and R^2 of 0.879, which are considered satisfactory. The GLASS surface daytime R_n data are filling values as long as the solar altitude is less than ~15°. Therefore, only CERES daytime R_n global land data were calculated within 50°S–50°N to match the annual GLASS data.

2.1.2. Surface R_n Reanalysis Data Sets

Three reanalysis R_n data sets were chosen for assessment and compared with the CERES R_n product due to their advantage with respect to spatiotemporal continuity and long records. The ERA-Interim (Dee et al., 2011), which is commonly used, was selected as mature reanalysis data set. A newer reanalysis data set, MERRA2 (Rienecker et al., 2011), was released in 2016 and needs assessment. The JRA-55 (Kobayashi et al., 2015) is one of the longest record reanalysis data sets and thus suitable for longtime climate change analyses. All of these reanalysis data sets imply four-dimensional variational analysis and feature different physical parameterizations (Decker et al., 2012). The ERA-Interim calculated radiation records based on the Rapid Radiation Transfer Model (Mlawer et al., 1997). The MERRA2 longwave radiative processes are described in Suarex and Chou (1994) and the shortwave radiative processes are based on Chou and Suarez (1999). The JRA-55 calculated longwave radiation fluxes via the band emissivity method with diffusivity approximation and shortwave radiation fluxes are computed by a two-stream method using the Delta-Eddington approximation (Joseph et al., 1976).

Some R_n products were not included in this study because of a variety of reasons. Satellite radiation products, such as the International Satellite Cloud Climatology Project (due to its sparse spatial resolution of ~280 km) or the Global Energy and Water Cycle Experiment (GEWEX; ends in 2007 and cannot match selected products), and other older assimilation models, such as ERA-40, MERRA, National Centers for Environmental Prediction-National Center for Atmospheric Research, and JRA-25 data sets, were not chosen. All selected gridded data used for assessment and uncertainty analysis were resampled to 1° latitude/longitude using nearest-neighbor interpolation. The metadata details are listed in Tables 1 and 2.

Table 2
Summary of Auxiliary Satellite Cloud Properties Used for Uncertainty Analysis

Name	Variable	Timespan	Spatial resolution	Temporal resolution
CERES SYN1deg Ed3A	Aerosol optical thickness; LWP, CP, WPR, IPED, CVOD, IWP and IE	2001.01–2015.12	1° × 1°	Monthly
CERES SSF1deg-lite_Ed2.6	LWP, CP, WPR, IPR, CVOD, IWP and IE	2001.01–2015.12	1° × 1°	Monthly

Note. LWP, liquid water path; CP, cloud phase; WPR, water particle radius; IPED, ice particle effective diameter; IPR, ice particle radius, CVOD, cloud visible optical depth; IWP, ice water path; and IE, infrared emissivity. The parameters are used only at the lowest sky level.

2.1.3. In Situ Observation Data

In situ observations measured by 15 networks were collected. The metadata for these measurement networks are provided in Table 3. The sites are globally distributed and characterize different land cover types in different climatic zones, as shown in Figure 1. Observations utilized for annual validation were aggregated from monthly observations only if there were no filled monthly values in one year. Only observations from 2001 to 2013 were used for validation.

2.1.4. Climate Zone Map

It has been shown that the accuracy of surface radiation data sets varies depending on different underlying surface types (Jia et al., 2016; Wang & Dickinson, 2013), which are directly determined by climate systems. Therefore, accessing the surface R_n in different climatic zones is required. Peel et al. (2007) updated the world map of the Koppen-Geiger climate classification. They calculated climate variables based on a large global data set of long-term monthly precipitation and temperature station time series. Considering the complex classification and limited site samples (Table 4), only five basic climatic zones (i.e., tropical, arid, temperate, cold, and polar) were adopted, as illustrated in Figure 1.

2.1.5. Land Cover Data

To characterize the spatial representativeness of each site, the MODIS land cover type product (MCD12Q1) was used to calculate the proportion of each site's land cover type located within 1°. Considering the overly detailed classification of the International Geosphere–Biosphere Program utilized in MCD12Q1, the original classification types were aggregated into seven types: forest, shrub, grassland, cropland, urban, ice/tundra, and barren land. We assumed that observed upward radiative fluxes were mainly influenced by the land cover type and the difference of the footprint size due to the instrument height was neglected. Because the site footprint covered a relatively homogeneous surface, observations represented radiative characteristics of the same land cover type in a pixel. Moreover, the land cover proportion of each site in a pixel was assumed to change minimally from 2001 to 2013. Therefore, the land cover proportion of each site in the corresponding pixel was calculated to characterize the site's spatial representativeness. Considering the significantly different radiative characteristics of the water surface, the impact of the water cover proportion in a pixel was also analyzed.

Table 3
Metadata for the 15 Measurement Networks Used in This Study

Abbreviation	Full name	Instrument	Observation years	Site number month/year	
La Thuile	Global Fluxnet (la Thuile Dataset)	CNR-1	1991–2008	183	150
CEOP	Coordinated Enhanced Observation Network of China	Eppley PIR, CG4	2007–2009	20	3
CERN	Chinese Ecosystem Research Network	CNR-1	2007	1	0
AsiaFlux	\	CNR-1	1999–2008	18	12
Game.Ann	GEWEX Asian Monsoon Experiment	EKO MS-0202F	1997–2003	6	1
SURFRAD	Surface Radiation Network	Eppley PIR, Spectrosun	1995–2013	7	7
BSRN	Baseline Surface Radiation Network	CMP21, Eppley PIR	1992–2012	5	5
ARM	Atmospheric Radiation Measurement	CNR-1	2002–2013	29	9
SMOSREX	Surface Monitoring of Soil Reservoir Experiment	CNR-1	2005–2010	1	1
CEOPInt	\	QMN101	2002–2009	1	1
ASIAQ	Asiaq- Greenland Survey		2008–2011	2	2
GC-Net	Greenland Climate Network	REBS Q* 7	1995–2012	5	4
HiWATER	\	CNR-4	2012	20	0
LBA-Eco	The Large-Scale Biosphere-Atmosphere Experiment in Ecology	REBS Q*7.1	1999–2006	10	2
SAFARI	A Southern African Regional Science Initiative		2000–2002	1	0
Total	\	\	\	309	197

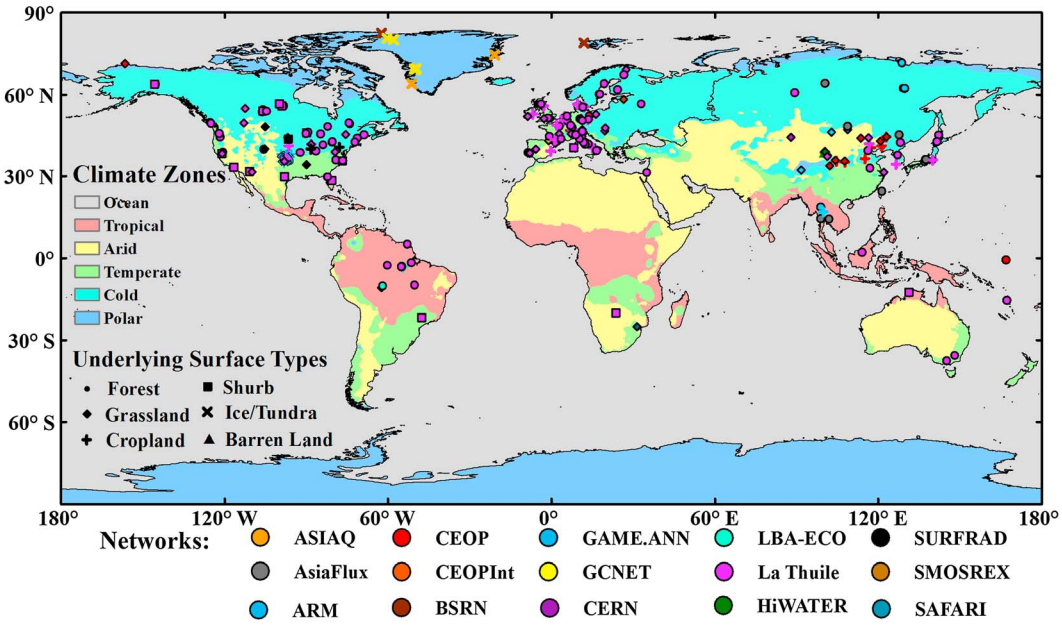

Figure 1. Global distribution of the 15 observation networks and climatic zones.

2.2. Methodology

2.2.1. In Situ Time Upscaling

Because ground sites were collected from various networks with different temporal resolutions and units, a consistent and strict preprocess method was carried out. After extreme records (records exceeding "physically possible" limits; Table 1 of Roesch et al., 2011) were excluded, daily observations were calculated only if measurement data were to be recorded every hour per day. For monthly observations, at least six days of data must be recorded every 10 days within one month (daily data should be recorded for more than 18 days in February). Annual observations were obtained by averaging all 12 monthly observations per year. Data not meeting these conditions were excluded. We unified the units of measurement to W m^{-2}. Previous studies showed that this method is trustworthy and provides strict data quality control (Jia et al., 2016; Jiang et al., 2014; Shi & Liang, 2013). Only monthly and annual validation was implemented because it is difficult for daily or weekly R_n variation to capture long-term climate change.

2.2.2. R_n Product Preprocessing

To match the validation time scale (monthly and annually), the R_n products with a temporal resolution of 3 hr (MERRA2 is hourly) were subhourly interpolated by bilinear interpolation and then transformed from Greenwich Mean Time to local time. The daily R_n was then obtained by averaging subhourly R_n products per day. The daytime R_n was also bilinearly incorporated and compared with the GLASS daytime R_n to verify global land R_n variations. Local sunrise and sunset times were determined using the exact location and day of year. Finally, the annual and monthly products were obtained by aggregating the daily results. The CERES EBAF only released monthly radiation products in local time; they were therefore sampled directly. We found that different higher-order interpolation methods have a limited impact on monthly and annual validation results due to time upscaling.

Table 4
List of Site Numbers Collected Monthly (Annual) in Different Land Cover Types and Climatic Zones

	Tropical	Arid	Temperate	Cold	Polar	Total
Forest	19 (12)	0 (0)	45 (37)	64 (48)	0 (0)	128 (97)
Shrub	1 (1)	2 (1)	9 (8)	7 (7)	0 (0)	19 (17)
Grassland	2 (0)	13 (6)	38 (18)	31 (22)	2 (1)	86 (47)
Cropland	2 (0)	20 (1)	17 (9)	23 (17)	0 (0)	62 (27)
Barren land	0 (0)	5 (1)	0 (0)	0 (0)	0 (0)	5 (1)
Ice/tundra	0 (0)	0 (0)	0 (0)	0 (0)	9 (8)	9 (8)
Total	24 (13)	40 (9)	109 (72)	125 (94)	11 (9)	309 (197)

2.2.3. Ground Measurement Uncertainty

Because satellite products and model data sets have gradually improved, it is no longer appropriate to disregard the measurement uncertainty during product assessment (Verma et al., 2016). Because most networks did not publish the uncertainty directly, the network uncertainties were determined based on their instruments. The accuracy of the daily totals of the CNR1 and CNR4 net radiometers, which have been widely used, is ±10% (https://www.campbellsci.com/; Table 3). In addition, Surface Radiation Network (SURFRAD), which

has a high calibration accuracy, claims that the accuracies achievable for shortwave measurements are ~2% for pyrheliometers and ~5% for pyranometers (±8% for R_n based on error propagation). Therefore, most network uncertainty differences are limited, except for GC-NET (5%–50% for R_n records; Steffen & Box, 2001). Taking time upscaling into consideration, we assumed that the monthly measurement random uncertainty is ±5% (±3% annually) and has a normal distribution; in addition, the uncertainty differences among ground networks are neglected, except for GC-NET (±25% monthly and ±15% annually). The measurement uncertainty was then introduced when calculating the deviation between in situ observations and product samples by using equation (4):

$$e_i = \frac{f}{0.5}(P_i - O_i), \tag{4}$$

where e_i is the modified deviation between products and in situ sites, f is the correction factor, P_i is the R_n product sample, and O_i is the ground observation for the ith pair. We assumed that O_i is the mean of the normal distribution. Because ±3.9 σ contains >99.99% of the normal probability distribution, we stipulated that f is 0.5 if the difference between P_i and O_i is larger than ±3.9 σ because the product error is much larger than the site uncertainty. If the deviation is within ±3.9 σ, f is equal to the definite integral between O_i and P_i, which means the closer P_i is to O_i, the more random uncertainty $P_i - O_i$ contains and the smaller f gets. Therefore, the deviation is more modified. If the deviation is 0, f is 0. More details about this method can be found in Harmel and Smith (2007).

2.2.4. Metrics for Validation

Four R_n products were sampled according to site locations and then compared with the site observations. The MBE, RMSE, and R^2 were chosen to characterize the surface R_n accuracy. The MBE, RMSE, and R^2 characterize the sample's overall bias, errors, and overall goodness of fit with a 1:1 line, respectively. Based on the modified deviation, the MBE, RMSE, and R^2 are calculated as

$$\mathrm{MBE} = \frac{\sum_{i=1}^{n}\left(\frac{f}{0.5}(P_i - O_i)\right)}{n} \tag{5}$$

$$\mathrm{RMSE} = \sqrt{\frac{\sum_{i=1}^{n}\left(\frac{f}{0.5}(P_i - O_i)\right)^2}{n}} \tag{6}$$

$$R^2 = 1 - \frac{\sum_{i=1}^{n}\left(\widehat{P}_i - \overline{O}\right)^2}{\sum_{i=1}^{n}\left(O_i - \overline{O}\right)^2}, \tag{7}$$

where n is the sample size and $\widehat{P}_i$ is the value of the samples fitted to the 1:1 line.

We assumed that the metric uncertainties of MBE and RMSE have a normal distribution, sampled 5,000 times by bootstrapping (Hillis & Bull, 1993), and then computed the mean and standard deviation. Site observations within the same grid at the same time were averaged in the climatic zone and overall validation.

2.2.5. Global Land Surface R_n Mean Values

To characterize the global land surface R_n variation, we calculated the global land surface R_n annual mean values using a latitude-weighted average. This method can minimize the influence of the real area difference among product grids at different latitudes. It is described mathematically as follows:

$$\overline{x} = \frac{\sum(x_i \cos(\theta_i))}{\sum \cos(\theta_i)}, \tag{8}$$

where $\overline{x}$ is the weighted average, x_i is the pixel value on the terrestrial surface, and θ_i is the latitude of the pixel value x_i.

2.2.6. Cloud Radiative Effect

To determine the R_n variation and detect its error source, the cloud radiative effect (CRE), which represents the cloud radiative forcing, was incorporated in the uncertainty analysis. The CRE is defined as

$$\mathrm{CRE} = F_{\mathrm{all}} - F_{\mathrm{clr}} \tag{9}$$

where F_{all} is the all-sky radiation flux and F_{clr} is the clear-sky radiation flux. The R_n and respective surface radiation fluxes are applicable.

2.2.7. Calculation of the Cloud Effective Radius

To check the anomalous CRE, several cloud parameters were detected. The CERES SYN1deg only released the cloud ice particle effective diameter, which is not directly comparable to the cloud ice particle effective radius (Ou et al., 1993). A transition method was provided (Minnis et al., 2011) and is defined as

$$r_e = \left(7.918\times10^{-9}\mu\mathrm{m}^{-2}D_e^2 + 1.0013\times10^{-3}\mu\mathrm{m}^{-1}D_e + 0.4441\right)D_e, \tag{10}$$

where r_e is the cloud ice particle effective radius and D_e is the ice crystal effective diameter.

3. Results Analysis

3.1. Validation Results at Individual Sites

From January 2001 to December 2013, in situ observations were collected at 309 sites for monthly validation. The validation results at individual sites show the accuracy of R_n products in particular areas that are meaningful for local-scale research. To reduce the influence of sample differences among sites, all monthly sites were mapped in Figure 2, except for sites with run time less than one year (257 sites remaining). The annual validation was neglected due to the limited sample size at each site.

The MBE and RMSE distributions show that all four R_n products have a better accuracy at midlatitude sites but higher uncertainty at higher latitudes. All four R_n products have a low R^2 at both low- and high-latitude sites. We calculated the spatial mean RMSE to determine the accuracy of each R_n product: CERES (19.96 ± 3.04 W m^{-2}), ERA-Interim (22.16 ± 3.28 W m^{-2}), MERRA2 (22.44 ± 3.27 W m^{-2}), and JRA-55 (24.27 ± 3.39 W m^{-2}).

The spatial representative effect was checked on the site scale. Because downward radiation fluxes are mainly related to atmospheric conditions that are relatively uniform on a monthly timescale, most global radiation validation work neglected the different spatial representation between sites and product pixels caused by the atmosphere (Kato et al., 2012; Wang & Dickinson, 2013; Zhang et al., 2015, 2016). Therefore, we assumed that R_n is mainly affected by the land cover proportion of each site on monthly and annual scales and carried out simple analysis (illustrated in Figure 3a). Considering that some sites are located in coastal regions and water and have radiative characteristics significantly different from land properties, the water cover proportion of site-located coastal grids (water cover proportion $>$ 0.1) was analyzed with the site RMSE in Figure 3b.

Figure 3 does not indicate a relationship between the site RMSE and land cover proportion but a significant correlation with the water cover proportion. The black line in Figure 3a is fitted to all scatters and shows an insignificant negative trend. We removed the plotted scatters in Figure 3a from left to right step by 0.05 land cover proportion and found that the refitted line (blue one) ceased to exhibit a negative trend once scatters below 0.15 were eliminated. The RMSE has a significant positive correlation with the water cover proportion (black line in Figure 3b). Using a similar scatter elimination method from right to left, we found that scatters below 0.40 exhibit a negative trend. Considering the surface heterogeneity and sample size, only sites with a land cover proportion below 15% or water cover proportion above 40% were removed from the climatic zones and overall validation (255 and 172 sites remained for monthly and annual validation, respectively). Ice sites in Figure 3 were neglected due to their high land cover proportions but low accuracies among all four products, which is very different compared with other land cover types.

3.2. Climatic Zone Validation Results

It is necessary to assess the surface R_n products of different climatic zones due to their complex environments. The monthly validation results are summarized in Table 5. The annual validation was neglected due to the limited sample size over tropical, arid, and polar regions.

Table 5 indicates that R_n products of different climatic regions show various accuracies. In tropical climatic zones, all R_n products have a significantly low R^2. This is likely due to frequent water vapor exchange and complex cloud conditions, two factors which make it difficult for satellite and reanalysis data sets to resolve atmospheric variation. Moreover, small R_n intermonthly variation is another reason for the lower R^2. The CERES product shows better validation results than the reanalysis data sets in arid areas. In temperate and cold climatic zones, all surface R_n products are highly accurate and CERES has the smallest RMSE. In polar

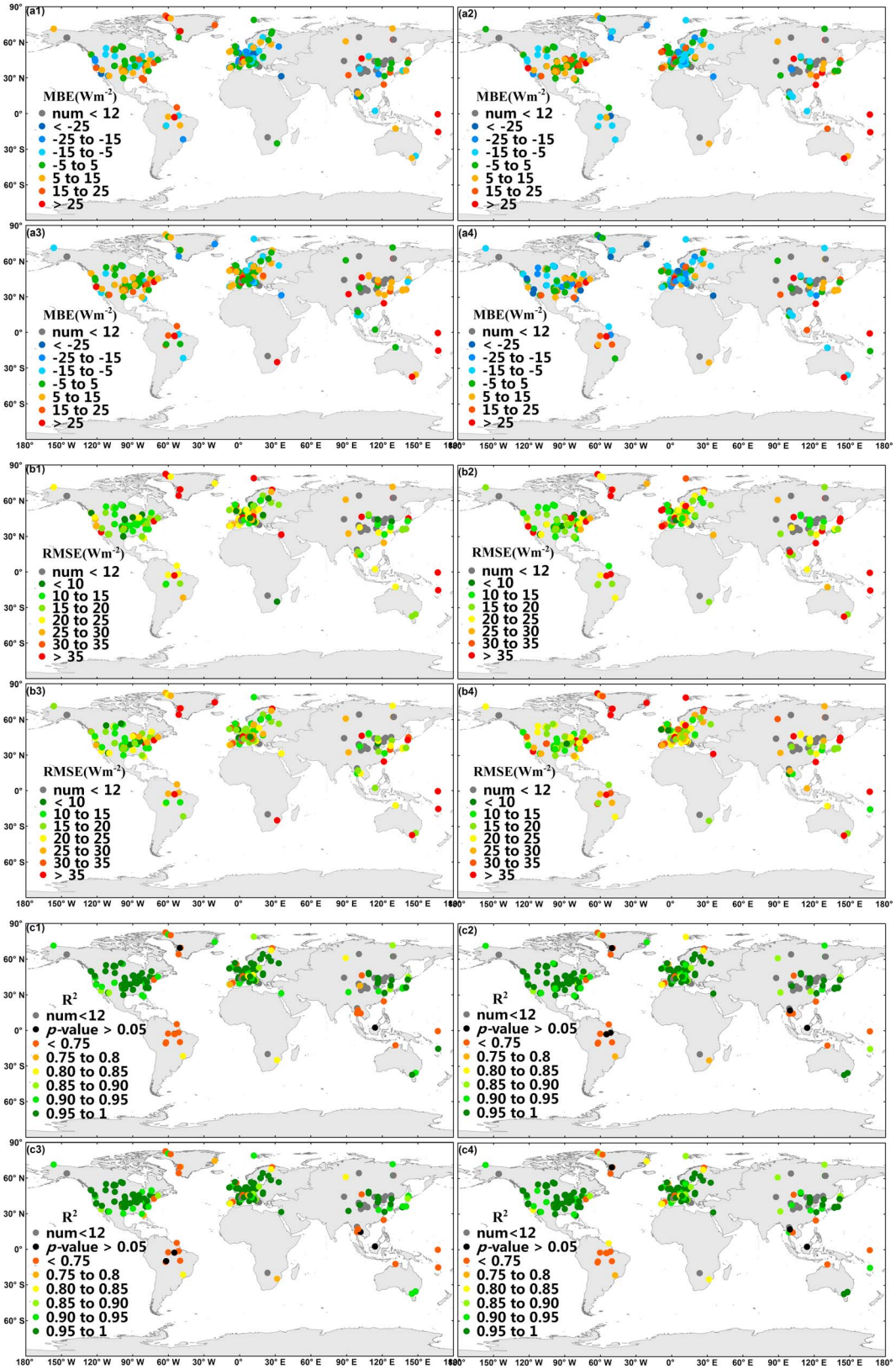

Figure 2. Spatial distribution of the validation results at each site. (a) MBE, (b) RMSE, and (c) R^2. The numbers 1–4 indicate CERES, ERA-Interim, MERRA2, and JRA-55, respectively. The *p*-value is the probability that extreme (nonlinear) events occur, representing the statistics significance.

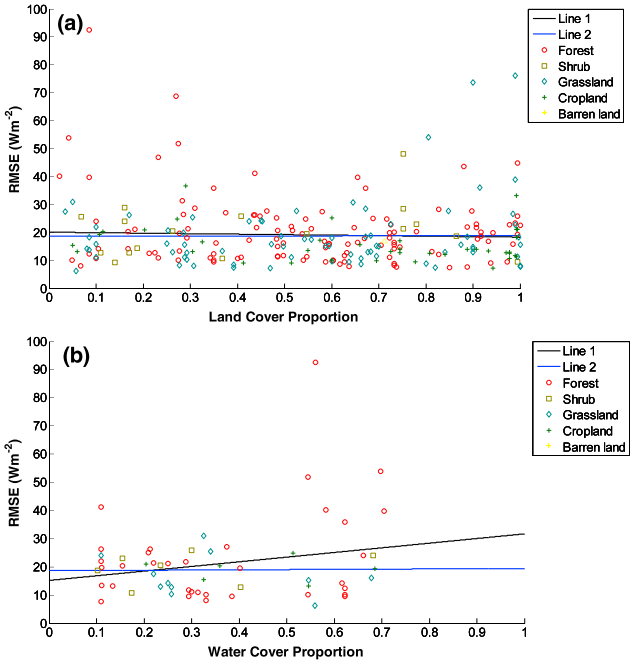

Figure 3. Scatterplot of the RMSE of each site and (a) land cover proportion and (b) water cover proportion on a monthly scale. All fitted lines are not significant at a *p*-value of 0.05, except for the black one in (b).

climatic regions, all R_n products have a high RMSE and low R^2 and the reanalysis data set values are much lower than the ground measurements. Zhang et al. (2016) reported that the downward shortwave flux bias of reanalysis data sets is lower than that of site observations above 60°N, which is due to biases of the cloud fraction in the reanalyses. It is difficult to use reanalysis data sets to model clouds without introducing active microwave observations (Walsh et al., 2009). The R^2 values in polar regions are somewhat higher than that in tropical regions because the products are in better agreement at these polar sites located at the margin of Greenland and Eurasia (Figure 2c) and have more notable seasonal variation compared with tropical sites. The sample size in tropical and arid areas is smaller than in other regions, which introduces more uncertainty to the validation results and influences R^2.

3.3. Overall Validation Results

Global validation is a direct way to assess the overall accuracy of each R_n product. The monthly validation density scatter diagrams are shown in Figure 4.

Figure 4 indicates that the four surface R_n products have a similar global accuracy on the monthly scale. The CERES EBAF samples are symmetrically distributed around the 1:1 line, and the data have an MBE of 2.40 ± 0.92 W m^{-2}; RMSE of 20.93 ± 1.54 W m^{-2}, which is the smallest; and R^2 of 0.87. Compared with CERES SYN1deg, the accuracy of the EBAF monthly R_n progressed modestly (Jia et al., 2016). The ERA-Interim data are predominantly lower than the 1:1 line at lower observed values, while the opposite is true at higher observed values. The ERA-Interim R_n shows an MBE of 2.35 ± 0.98 W m^{-2} with an RMSE of 22.36 ± 1.52 W m^{-2} and R^2 of 0.89. The MERRA2 R_n is predominately higher than the 1:1 line, except for the observed low quantity (<50 W m^{-2}). It has an MBE of 7.05 ± 0.99 W m^{-2}, which is a little bit higher; RMSE of 23.52 ± 1.49 W m^{-2}; and R^2 of 0.89, which is the best. The JRA-55 R_n is lower than the 1:1 line especially for lower observed values (<50 W m^{-2}). The JRA-55 R_n has an MBE of −1.57 ± 1.15 W m^{-2}; RMSE of 26.28 ± 1.53 W m^{-2}, which is largest; and R^2 of 0.87. The CERES EBAF surface R_n shows the best performance, while the ERA-Interim and MERRA2 R_n data sets show fewer significant accuracy differences from the satellite product and the JRA-55 R_n data set has a slightly lower accuracy. These results interrelate with the individual site validation. The overall annual results are illustrated in Figure 5.

Figure 5 indicates that the four surface R_n products have no notable accuracy differences on the annual scale. The ERA-Interim R_n product performs slightly better, with the smallest RMSE of 13.06 ± 2.70 W m^{-2} and R^2 of

Table 5
Monthly Validation Results for Different Climatic Zones

		Tropical (n = 360)	Arid (n = 511)	Temperate (n = 2872)	Cold (n = 3629)	Polar (n = 625)
MBE (W m^{-2})	CERES	7.12 ± 4.23	6.71 ± 3.95	−1.13 ± 1.63	0.48 ± 1.37	14.39 ± 6.22
	ERA-Interim	−2.77 ± 5.14	6.72 ± 4.15	2.29 ± 1.48	3.92 ± 1.55	−6.61 ± 5.21
	MERRA2	5.75 ± 5.06	15.89 ± 4.32	5.82 ± 1.55	7.94 ± 1.55	−1.12 ± 5.85
	JRA-55	10.32 ± 5.11	−3.10 ± 5.81	−3.22 ± 1.83	0.10 ± 1.70	−9.71 ± 7.61
RMSE (W m^{-2})	CERES	20.60 ± 3.29	21.80 ± 6.62	19.91 ± 2.82	19.14 ± 2.12	38.88 ± 6.57
	ERA- Interim	23.47 ± 4.37	22.93 ± 7.11	20.73 ± 2.98	21.53 ± 2.27	30.76 ± 7.39
	MERRA2	23.72 ± 4.26	27.70 ± 7.64	19.92 ± 2.84	23.05 ± 2.22	34.26 ± 6.46
	JRA-55	25.27 ± 3.95	30.33 ± 6.66	22.28 ± 2.67	23.76 ± 2.34	45.77 ± 6.54
R^2	CERES	0.36*	0.85*	0.88*	0.89*	0.67*
	ERA- Interim	0.29*	0.86*	0.90*	0.90*	0.68*
	MERRA2	0.17*	0.84*	0.91*	0.89*	0.67*
	JRA-55	0.32*	0.75*	0.88*	0.88*	0.65*

*p-value < 0.01.

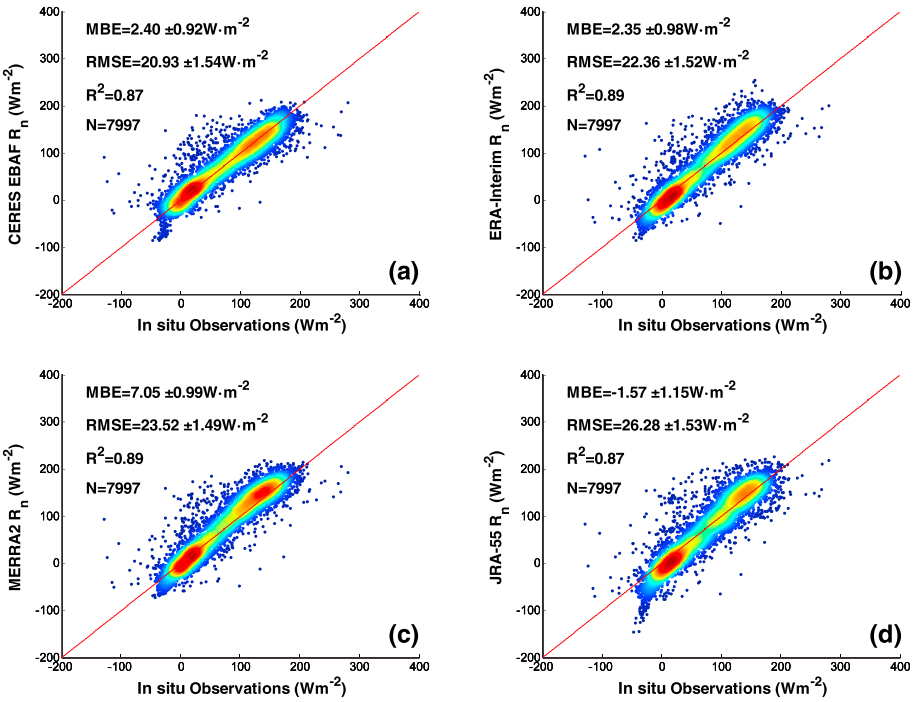

Figure 4. Density scatter plots for monthly in situ samples and four surface R_n products: (a) CERES; (b) ERA-Interim; (c) MERRA2; and (d) JRA-55. The R^2 values of the four R_n products are significant with a p-value <0.01. The warm colors represent the high density of samples, while the cool colors represent low density.

0.83. The RMSE values of CERES EBAF and MERRA2 R_n are slightly higher than that of ERA-Interim. The MERRA2 R_n is still higher than the in situ observations, while the JRA-55 R_n is lower. Compared with the monthly results, the overall annual R_n validation results have a greater uncertainty resulting from fewer samples.

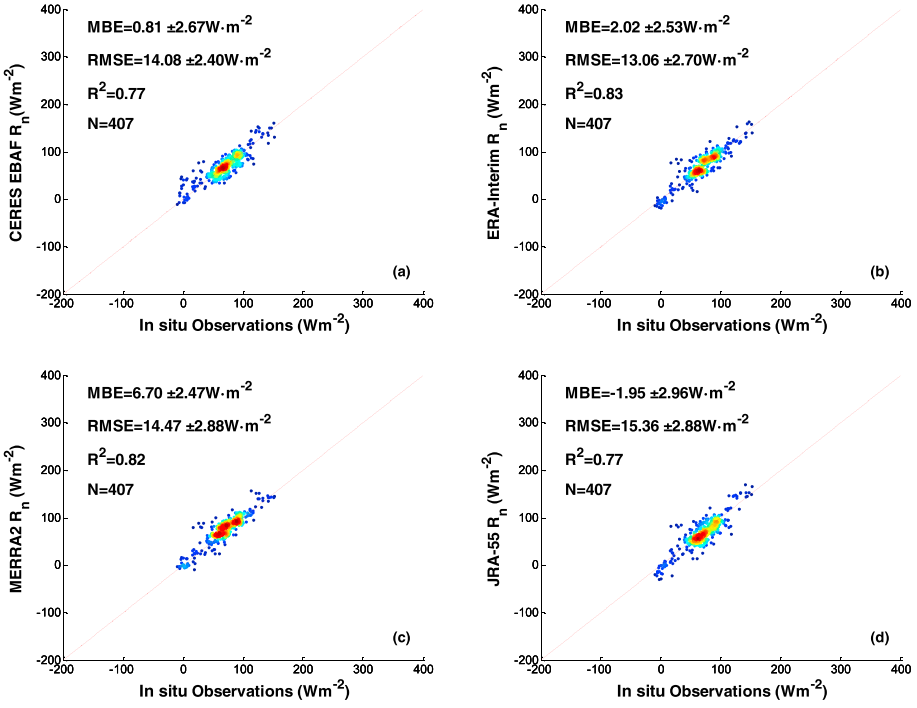

Figure 5. Density scatter plots for annual in situ samples and four surface R_n products: (a) CERES, (b) ERA-Interim, (c) MERRA2, and (d) JRA-55. The R^2 values of the four R_n products are significant with a p-value <0.01. The warm colors represent the high density of samples, while the cool colors represent low density.

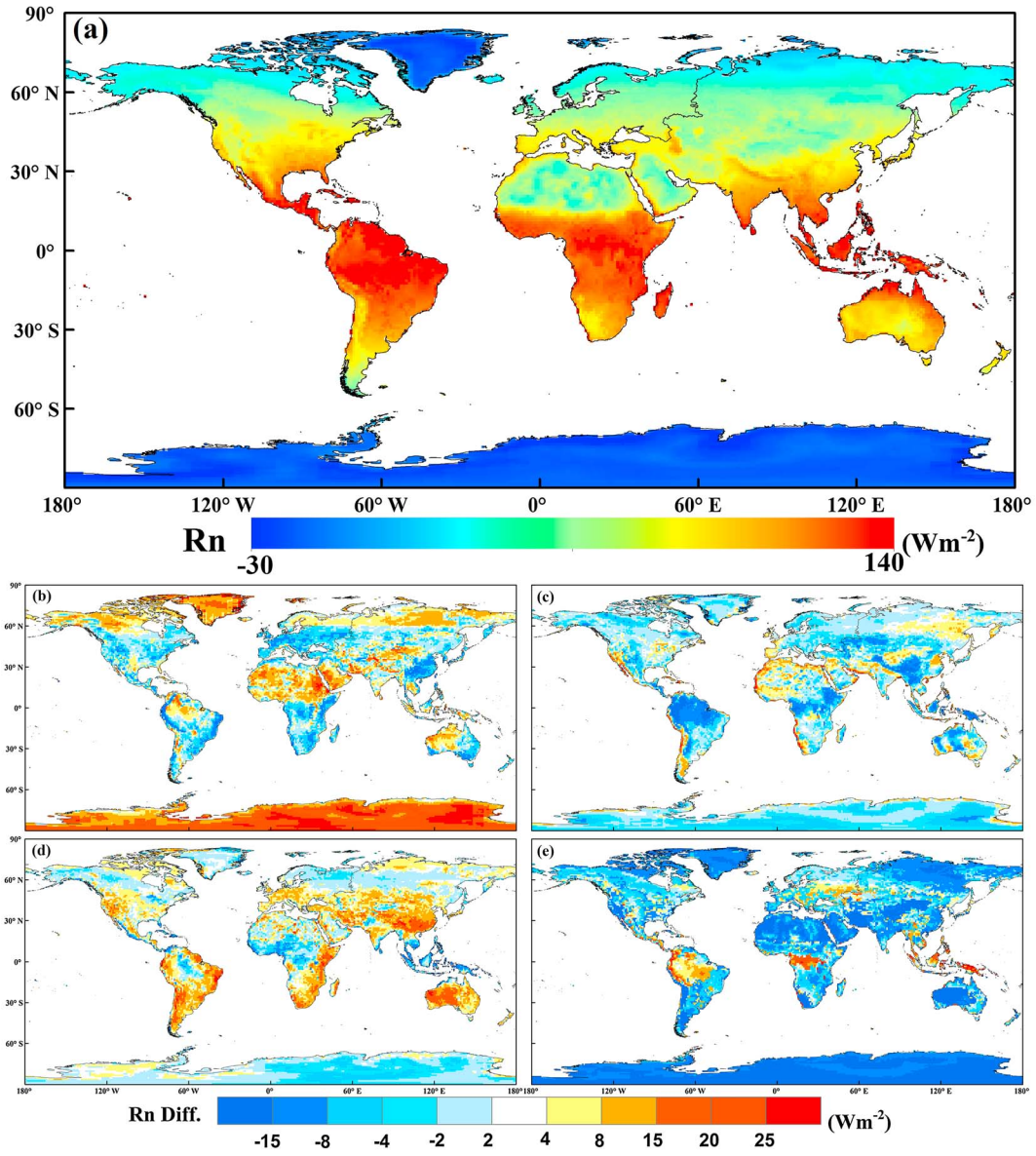

Figure 6. Spatial distribution of the mean annual surface R_n difference. (a) all-product annual mean; (a) subtracted from (b) CERES EBAF; (c) ERA-Interim; (d) MERRA2; and (e) JRA-55.

These four surface R_n products show no significant accuracy differences on two temporal scales based on global in situ observations. The monthly RMSE range of the four products is 5.35 W m^{-2}, and the annual range is 2.30 W m^{-2}. The accuracy assessed using this validation method is the total error including errors caused by spatial and temporal sampling mismatch and modeling errors (Kato et al., 2012). The uncertainty in the CERES EBAF global annual mean R_n was determined to be 12 W m^{-2} using the sensitivity study of the radiative transfer model input. Ground measurements were also used for comparison with gridded samples; the validations match the uncertainty results. However, it is difficult to use the sensitivity study to comprehensively assess several surface R_n products.

3.4. Spatial-Temporal Comparison

Because these R_n products have a similar overall accuracy but varying accuracies and systematic biases across different climatic zones, a detailed spatiotemporal comparison was necessary. The simply averaged annual mean values of all R_n products from 2001 to 2013 were calculated (Figure 6a). The differences in the annual mean of each product and the all-product annual mean values are shown in Figures 6b–6e.

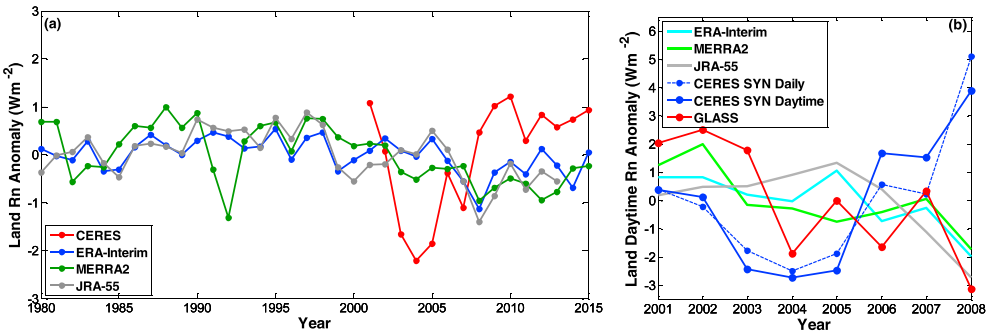

Figure 7. Annual land surface (a) R_n anomalies and (b) daytime R_n anomalies. The CERES SYN1deg daily R_n aggregated annual variation is also added to (b) as a reference.

The surface R_n products show a varying R_n difference distribution compared with the all-product annual mean. The CERES EBAF R_n product is much higher over both the polar and desert areas. Gupta et al. (2010) also found that the CERES SSF R_d^l was overestimated over desert regions due to the overestimation of input air temperature and humidity profiles, which still exists in SYN1deg R_d^l (Wang & Dickinson, 2013). The ERA-Interim R_n is lower over low-latitude areas and the Tibet Plateau. The MERRA2 R_n is higher over land, especially in southern China, western Australia, and eastern Brazil. The JRA-55 R_n is predominately lower over most of the land but higher over near-equator regions. The distribution maps support the climatic zone validation results. To check the variation consistency of the R_n products of long time series, the annual R_n anomaly variation is shown in Figure 7a.

All reanalysis data sets have similar temporal variations in the land surface R_n, while the CERES EBAF product shows a significantly different trend from 2001 to 2008. It has a valley-type temporal variation, containing a sharp decline of 3.28 W m^{-2} from 2001 to 2004, a range even larger than the impact caused by the eruption of Mount Pinatubo modeled using the MERRA2 in 1991. Furthermore, from 2005 to 2008, the CERES EBAF product increased by 2.67 W m^{-2}, which is inversely related to the reanalysis data set results.

To further evaluate the land surface R_n temporal variation from 2001 to 2008, we included the GLASS surface daytime R_n product, which is a new product directly estimated from satellite observations without relying on other ancillary information from clouds and aerosols. The GLASS daytime R_n shows an average RMSE of 31.61 W m^{-2}, average bias of −17.59 W m^{-2}, and R^2 of 0.879 (Jiang et al., 2016). The GLASS product suite focuses on long-term data records based on multiple satellite observations and also takes advantage of existing high-level satellite products (Liang et al., 2013, 2014). All products were converted to daytime values, and a comparison is shown in Figure 7b.

The CERES SYN1deg land surface daytime R_n data show an inconsistent trend compared with the GLASS R_n product and other reanalysis data sets. Because daytime R_n data are closely correlated to daily R_n, we infer that the CERES EBAF annual variations also do not match the GLASS R_n data. Although the CERES EBAF R_n shows an accuracy comparable to other products based on global validation using ground measurements, the temporal variations are significantly different.

As one of most advanced radiation products, CERES accumulated a sufficiently lengthy time series record and plays an important role in analyses of global surface energy budget variations and climate feedback. Thus, it is necessary to explore reasons for the inconsistent trend. Uncertainty analysis of the CERES land surface R_n data was carried out and the results are as follows.

4. Uncertainty Analysis of the CERES R_n Product

Based on the CERES EBAF surface R_n product, a valley-type temporal variation in the global land R_n from 2001 to 2008 was observed, while it has not been detected over surface ocean and TOA land (Figure 8a). It contains a sharp decline of 3.28 W m^{-2} from 2001 to 2004, primarily dominated by longwave net radiation (R_n^l; Figure 8c). After inspecting details of the radiation components (Figures 8b–8g), we found striking changes, including an increase in the surface land upward longwave radiation (R_u^l) of 1.67 W m^{-2} from 2001 to 2002 (Figure 8g) and a

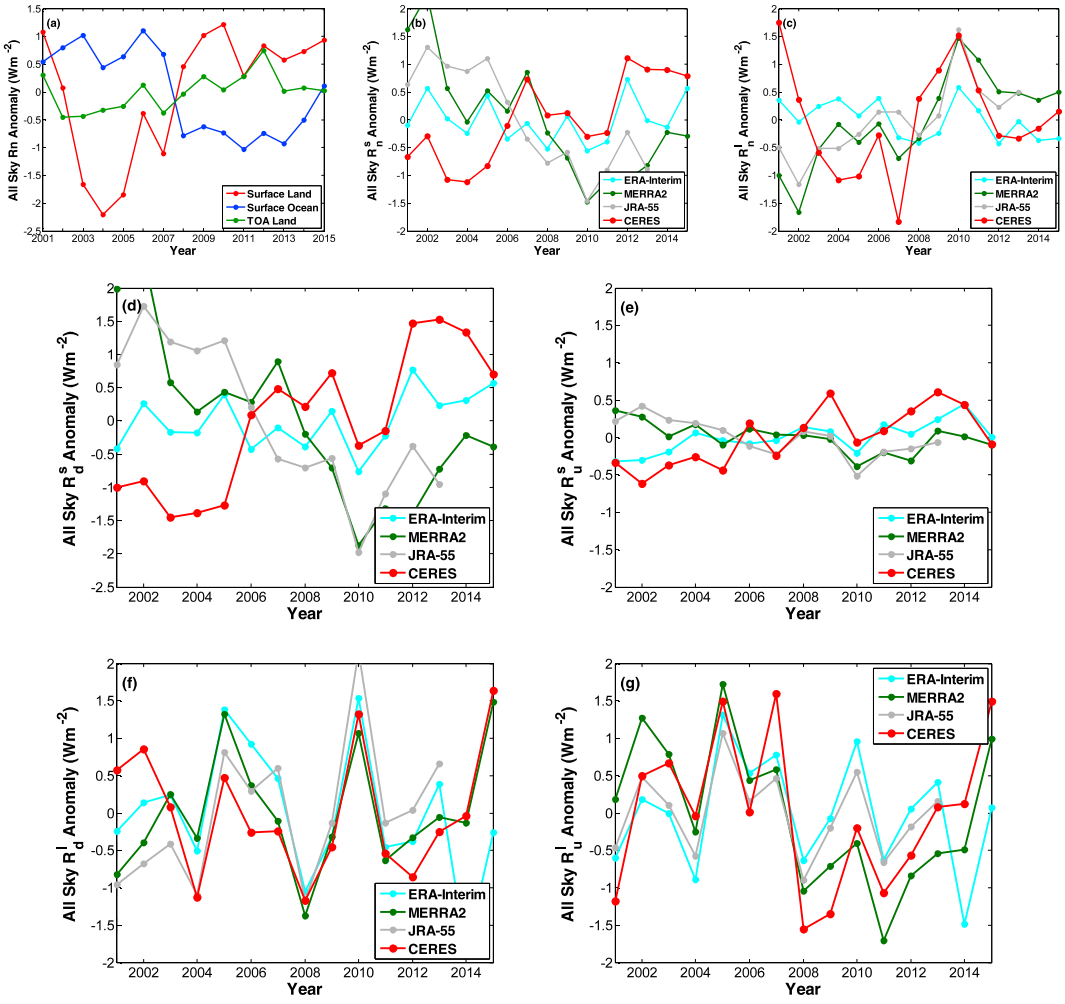

Figure 8. Annual anomalies of (a) R_n, (b) R_n^s, (c) R_n^l, (d) R_d^s, (e) upward shortwave radiation (R_u^s), (f) R_d^l, and (g) R_u^l of each R_n product.

decrease in downward longwave radiation (R_d^l) of 1.98 W m^{-2} from 2002 to 2004 (Figure 8f), which were not found in R_n reanalysis data sets. The R_n then increased by 2.67 W m^{-2} from 2004 to 2008, affected by both net shortwave radiation (R_n^s) and net longwave radiation (R_n^l; Figures 8b and 8c). A unique increase of 1.35 W m^{-2} in the surface land downward shortwave radiation (R_d^s) from 2005 to 2006 (Figure 8d) and significant decrease of 3.15 W m^{-2} in the surface land R_u^l from 2007 to 2008 were determined (Figure 8g). The significant negative global land surface R_n anomaly is a combination of four component changes from 2001 to 2008.

Furthermore, to check the magnitude of the valley-type variation of the CERES R_n and respective component variation on the regional scale, the annual difference distributions for 2004 minus 2001 and 2008 minus 2004 are shown in Figure 9. The figure shows that in addition to some parts of Africa and south America, the R_n decreased dramatically worldwide (Figure 9a) from 2001 to 2004. In particular, it declined by more than 10 W m^{-2} in Australia, northern Canada, and the Malay Archipelago. The extensive decrease of R_n was mainly affected by R_u^s and R_u^l in Eurasia and Oceania (Figures 9e and 9i). In southeastern South America, the R_d^s predominately decreased and affected the R_n (Figure 9c). Conversely, the R_n annual difference for 2008 minus 2004 (Figure 9b) demonstrates that R_n escalated predominantly in most areas, increasing by almost 18 W m^{-2} in Greenland, eastern Brazil, and western Africa. The R_d^s increase played a vital role in the R_n increase at middle and high latitudes of the Northern Hemisphere (except for Greenland). The R_n increase over South America and Africa is due to the combined influence of short- and longwave radiation.

As the surface radiation budget, R_n is affected by the radiation component uncertainty determined by several input factors. Aerosols are one of the main factors impacting R_d^s. The data quality summary for CERES EBAF

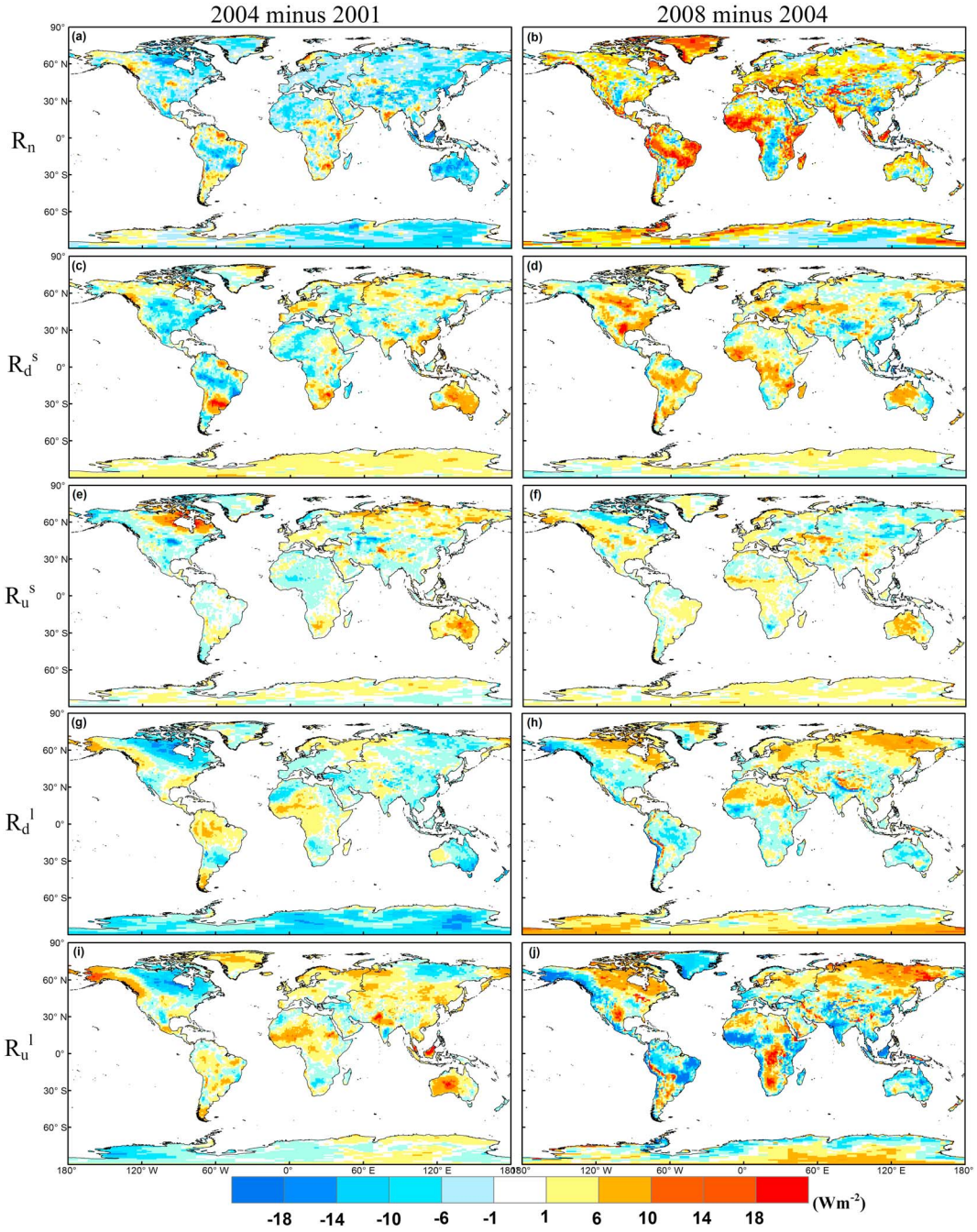

Figure 9. Spatial distribution of the land surface annual difference for CERES EBAF (a and b) R_n, (c and d) R_d^s, (e and f) R_u^s, (g and h) R_d^l, and (i and j) R_u^l. (a, c, e, g, and i) are 2004 minus 2001 and (b, d, f, h, and j) are 2008 minus 2004.

surface products mentions that a discontinuity and spurious trend appear in the time series of the clear-sky surface insolation flux due to MODIS-derived aerosol optical thickness (AOT) inputs changing from Collections 4 to 5 in 2006. The aerosol model of C5 was modified by measurements and the AOT of C4 generally exceeds that in C5 on land (Li et al., 2007). Based on the MODIS-derived AOT data from CERES SYN1deg, the discontinuity also affected the all-sky EBAF surface R_d^s (Figure 10a).

In addition, as a primary input of CERES EBAF, CERES SYN1deg was retrieved by two sources of temperature and humidity profiles, which were switched from GEOS-4.1 to GEOS-5.2.0 in January 2008, generating a discontinuity (Figure 10d) in the time series of TOA and surface longwave radiation (Doelling et al., 2013). The MODIS cloud retrieval algorithm was less reliable at night because cloud retrievals are solely based on

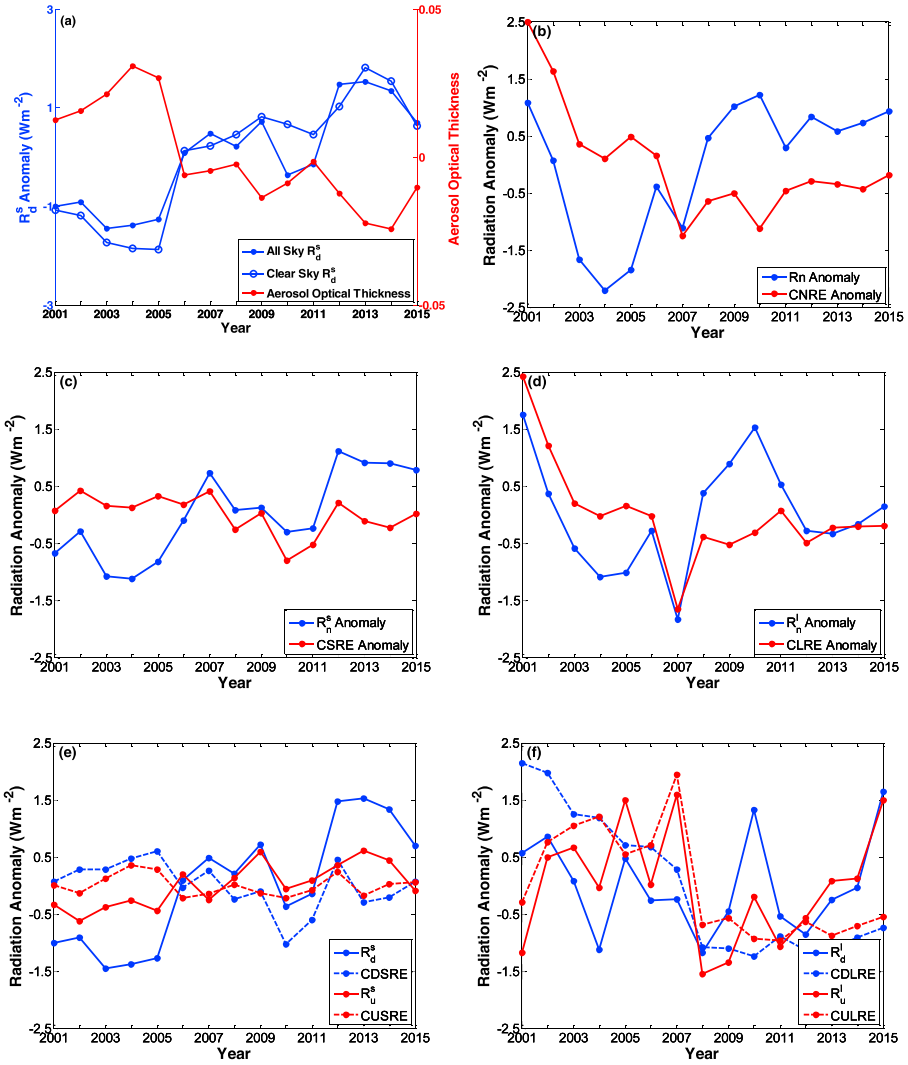

Figure 10. Annual anomalies in CERES (a) AOT, clear-sky and all-sky surface R_d^s; (b) surface R_n and cloud R_n effect (CNRE); (c) surface R_n^s and cloud shortwave R_n effect (CSRE); (d) R_n^l and cloud longwave R_n effect (CLRE); (e) R_d^s, cloud downward shortwave radiation effect (CDSRE), R_u^s, and cloud upward shortwave radiation effect (CUSRE); (f) R_d^l, cloud downward longwave radiation effect (CDLRE), R_u^l, and cloud upward longwave radiation effect (CULRE) over the global land surface.

infrared MODIS channels. Therefore, the nighttime longwave radiation retrieval relies more heavily on assimilated meteorological data. While comparing the CERES SYN1deg R_n, we found that the SYN1deg daytime R_n intensified the discontinuity in 2006 and weakened the discontinuity in 2008 (Figure 7b). This strengthens our inference because the nighttime effect of atmospheric profiles was weakened and the daytime effect of the aerosol visible depth was enhanced. In addition, CERES is an end-to-end processing system. Therefore, CERES cloud products, which are the essential input of CERES surface radiation retrievals, were also affected by discontinuities in the temperature, wind, and humidity profiles from GEOS-4.0 to GEOS-5.0 in January 2008 (Minnis et al., 2011). Hence, the discontinuity in the all-sky land R_u^l in 2008 was influenced by the cloud effect from upward longwave radiation (Figure 10f). Although EBAF used GEOS-5.4.1 as a reference to largely mitigate the discontinuity in the clear-sky R_d^l, the jump from 2007 to 2008 in the all-sky R_n^l remains (Figure 8c).

The cloud information, determining the CRE (defined in section 2.2.6) and affecting the all-sky surface R_n, was evaluated. The decline in the land surface R_n from 2001 to 2004 was predominately affected by the cloud net radiation effect of 2.14 W m^{-2} in the former two years (Figure 10b). The cloud longwave net radiation effect was particularly affected, with a decline of 2.23 W m^{-2} (Figures 10d and 10f).

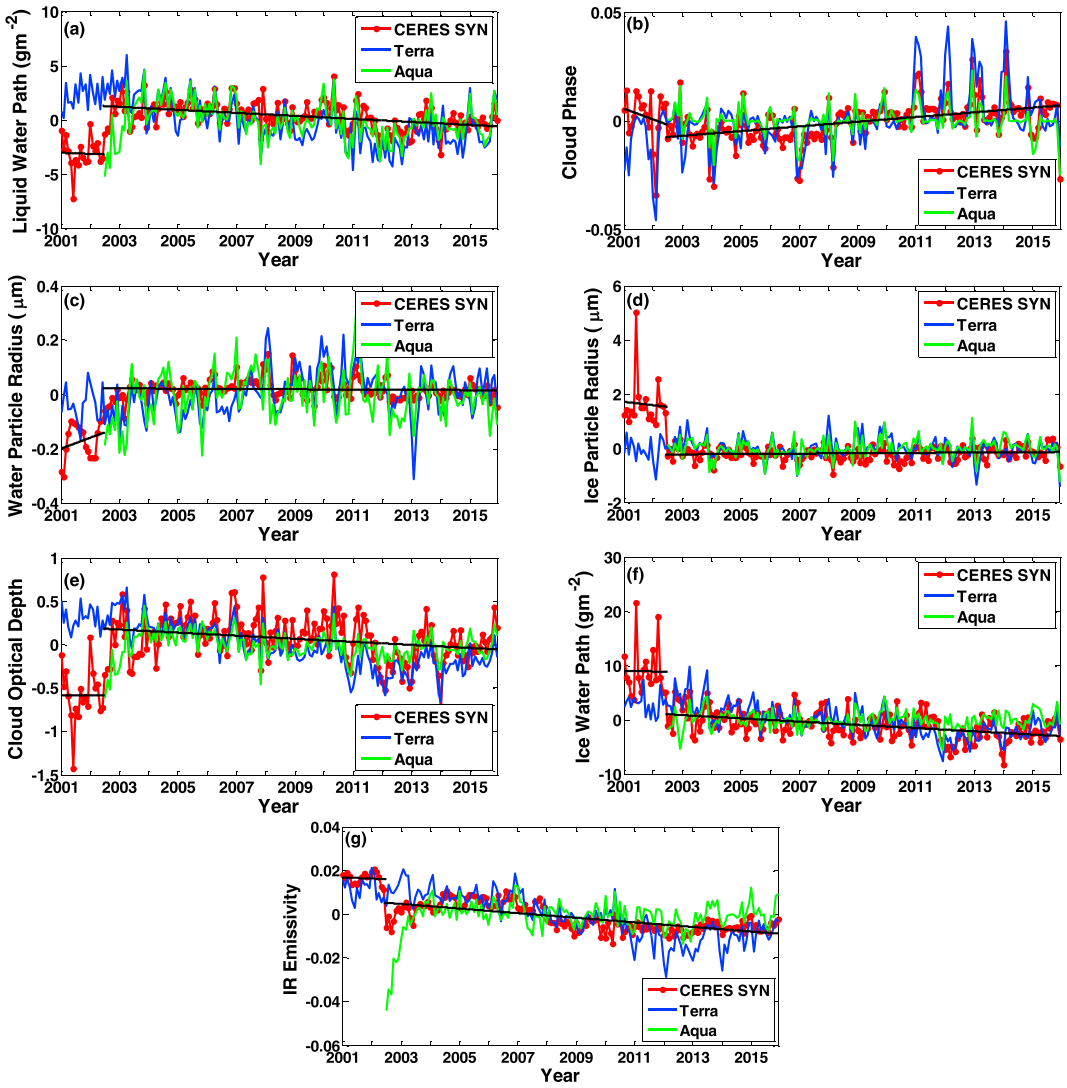

Figure 11. Comparison of monthly anomalies for averaged land (a) liquid water path, (b) cloud phase, (c) water particle radius, (d) ice particle radius, (e) ice water path, (f) cloud visible optical depth, and (g) infrared emissivity of SYN1deg for Terra and Aqua.

Based on CERES SYN1deg low-sky cloud properties, 12 types of cloud parameters were analyzed, all of which characterize cloud properties and are essential for all-sky surface radiation retrievals. Seven parameters demonstrated a notable anomaly in 2001 and 2002 in the lower sky (Figures 11a–11g). Moreover, the cloud parameters of SYN1deg are contradictory to that from SSF1deg in 2001–2002. Based on the comparison of the Terra and Aqua low-sky cloud parameters released by CERES SSF1deg, the cloud parameters from Terra did not exhibit significant anomalies before July 2002, while the three cloud products matched each other very well after December 2002 (Figures 11a–11g). The results from SYN1deg and SSF1deg contradict each other in that the two cloud product versions have a widely different trend, although they mainly utilize the same satellite observation inputs. The SYN1deg cloud retrieval (Minnis et al., 2011) derives cloud properties measured by MODIS twice daily from March 2000 through June 2002 (Terra only) and four times daily after July 2002 (Terra plus Aqua), but the SSF1deg cloud retrieval keeps single-satellite observations. It might have given rise to the discontinuity of the cloud information, causing the spurious cloud parameter variation of the SYN1deg, finally affecting the cloud longwave net radiation effect and surface R_n in 2001 and 2002.

We conclude that the temporally interpolated methods from the SYN1deg cloud products have not completely eliminated the impact of the discontinuity caused by adding Aqua observations in July 2002.

Furthermore, there is a higher cloud uncertainty between Terra and Aqua in 2002, both of which caused a suspicious cloud net radiation effect anomaly in 2001 and 2002 (Figure 11g), finally causing the surface R_n significant decrease in 2001 and 2002. Because the SYN1deg did not change the GEO observation sensors in 2002 (Doelling et al., 2013), the GEO data sources are not the main reason of detected anomalous cloud parameter variation. Moreover, the version update of MODIS regarding the AOT generated discontinuities both before and after 2006. The temperature and humidity profiles switch in January 2008 also led to global discontinuities in the land surface R_n. Anomalous R_n values from 2003 to 2005, which normally vary but are significantly low, are due to the contrast with the anomalous decrease from 2001 to 2002 and two notable increases in 2006 and 2008.

5. Conclusions

Although some regional and preliminary validations of the surface R_n products have been previously published, there is a lack of a comprehensive validation and intercomparison of multiple global R_n products in the community. In this study, surface measurements were performed at 309 global sites to validate the CERES EBAF and three reanalysis R_n data sets, including ERA-Interim, MERRA2, and JRA-55, on both monthly and annual time scales.

The individual monthly validation indicates that the four R_n products show a better accuracy at midlatitude sites but higher uncertainty at higher latitudes. The monthly validations for different climatic zones indicate that the four R_n products have a low R^2 over tropical regions and a limited accuracy over polar regions, where reanalysis data set R_n values are generally lower than the ground observations. The MERRA2 R_n product is predominately higher than ground measurements in most areas, except for polar regions, and the JRA-55 R_n has lower values, except for tropical regions.

The overall results indicate that the accuracies of these four R_n products on both time scales are not significantly different. The RMSE range is 5.35 W m^{-2} (the RMSE range is 2.59 W m^{-2} without JRA-55) on a monthly scale and 2.30 W m^{-2} (1.41 W m^{-2} without JRA-55) on an annual scale. On the monthly scale, the CERES EBAF R_n product is more accurate, with uniform scattering; the RMSE of 20.93 ± 1.54 W m^{-2} is the smallest. On the annual scale, the ERA-Interim R_n product performed slightly better with the smallest RMSE of 13.06 ± 2.70 W m^{-2}. On both temporal scales, the MERRA2 R_n product has higher values, while the JRA-55 R_n has lower values than the in situ observations.

The intercomparison of these four R_n products showed significant differences. Compared with the mean values of these four products, the CERES EBAF R_n product has higher values over high-latitude and desert regions (e.g., northern Africa); the ERA-Interim R_n product has lower values over low latitudes and the Tibet Plateau. The MERRA2 R_n has higher values than the mean values of the four products over land, especially in southern China, western Australia, and eastern Brazil. The JRA-55 R_n has lower values over most land surfaces but higher values near the equator. When examining the average annual variations of these four R_n products, we found that the three reanalysis data sets were similar and the CERES EBAF R_n product had a significantly different trend from 2001 to 2008, consisting of a decline of 3.28 W m^{-2} from 2001 to 2004 and increase of 2.67 W m^{-2} from 2004 to 2008. When compared with the GLASS daytime R_n product, the CERES SYN1deg R_n annual average anomaly still exists.

A detailed uncertainty analysis was carried out. The R_n annual average anomaly was found only over land in the CERES EBAF. Moreover, the annual land surface demonstrates that the R_n dramatically decreased worldwide from 2001 to 2004. From 2004 to 2008, the R_n increased in most areas, by almost 18 W m^{-2} in Greenland, eastern Brazil, and western Africa. When examining the input data for the CERES EBAF R_n product, we found that using input products from different versions is the main cause of the anomalies. Changing the MODIS-derived AOT from Collections 4 to 5 resulted in the discontinuity in the global land downward shortwave radiation in 2006, and the switch of the temperature and humidity profiles from GEOS-4.1 to GEOS-5.2.0 in January 2008 generated a discontinuity in the time series of surface longwave net radiation over land. The switch of the GEOS versions also affected the cloud products from SYN1deg and caused a discontinuity in the cloud longwave net radiation in 2008. These two input switches caused a significant R_n increase in 2006 and 2008.

The notable decline in the land R_n from 2001 to 2004 was mainly caused by the anomalous cloud longwave net radiative effect in 2001 and 2002. When analyzing low-sky cloud parameters from SYN1deg, seven types of parameters had a significant monthly anomaly before July 2002, which were not found in the Terra retrieval results from the SSF1deg. Furthermore, some cloud parameters had a higher uncertainty in 2002 when comparing Terra and Aqua SSF1deg cloud products. The addition of Aqua observations in July 2002 caused a discontinuity and high cloud retrieval uncertainty in 2002 that led to the spurious trend in cloud longwave net radiation effects, finally affecting the surface R_n in 2001 and 2002.

Because separate surface radiation component retrievals introduce more errors to the surface R_n, it may be preferable to directly estimate the R_n. Reanalysis radiation transfer models can constrain the surface irradiances by introducing satellite TOA observations. Because surface R_n data still have large uncertainties, numerical models and satellite retrieval methods urgently need improvement. The validation of R_n products still requires constructing and maintaining comprehensive high-precision observation networks. However, the validation may not be able to reveal all potential issues because of large uncertainties in these R_n products. This study demonstrates that temporal analysis can be a powerful complementary tool that may enable us to identify potential quality issues in global products.

Acknowledgments

This study was partially supported by the Chinese Grand Research Program on Climate Change and Response (projects 2016YFA0600101 and 2016YFA0600103) and the National Natural Science Foundation of China under Grant 41331173. We gratefully acknowledge the CERES science team (https://ceres.larc.nasa.gov), GLASS team (http://glass-product.bnu.edu.cn/introduction/allwave.html), ECMWF international modeling groups (http://apps.ecmwf.int/datasets/), MERRA2 science team (https://gmao.gsfc.nasa.gov/reanalysis/MERRA-2/), and Japan Meteorological Agency (http://jra.kishou.go.jp/JRA-55/index_en.html#jra-55/) for providing data. This study used eddy covariance data acquired by the FLUXNET community (http://www.fluxdata.org/) and the following networks: ARM (http://www.archive.arm.gov/), AsiaFlux (http://www.asiaflux.net/), ASIAQ, BSRN (http://bsrn.awi.de/), CEOPInt, CEOP, CERN (http://www.cerndata.ac.cn/), GC-Net (http://cires1.colorado.edu/science/groups/steffen/gcnet/), HiWATER, GAME ANN (http://www.hyarc.nagoya-u.ac.jp/game/phase-1/game-aan.html), LBA (http://www.lbaeco.org/), SAFARI (http://daac.ornl.gov/S2K/safari.shtml), SMOSREX (http://www.cesbio.ups-tlse.fr/), and SURFRAD (http://www.esrl.noaa.gov/gmd/grad/surfrad/). We thank the reviewers and Wenshan Wang for their comments about site accuracy issues and the tilt correction of the GC-NET network. We acknowledge the financial support for eddy covariance data harmonization provided by the CarboEuropeIP, FAO-GTOS-TCO, Ileaps, Max Planck Institute for Biogeochemistry, National Science Foundation, University of Tuscia, Université Laval, Environment Canada, and U.S. Department of Energy. We acknowledge the data set development and technical support from the Berkeley Water Center, Lawrence Berkeley National Laboratory, Microsoft Research eScience, Oak Ridge National Laboratory, University of California–Berkeley, and University of Virginia. We also would like to thank Yan Li and Ran Li from the Xinjiang Institute of Ecology and Geography, CAS, and Jean Christophe Calvet from CNRM-GAME for sharing data.

References

Bretherton, C. S., & Battisti, D. S. (2000). An interpretation of the results from atmospheric general circulation models forced by the time history of the observed sea surface temperature distribution. *Geophysical Research Letters*, *27*(6), 767–770. https://doi.org/10.1029/1999GL010910

Bye, J., Fraedrich, K., Kirk, E., Schubert, S., & Zhu, X. (2011). Random walk lengths of about 30 years in global climate. *Geophysical Research Letters*, *38*, L05806. https://doi.org/10.1029/2010GL046333

Chou, M. D., & Suarez, M. J. (1999). A solar radiation parameterization for atmospheric studies, NASA TM-104606 (NASA Technical Memorandum 104606, vol. 15, 40 pp.).

Cruz, F. W., Burns, S. J., Karmann, I., Sharp, W. D., Vuille, M., Cardoso, A. O., et al. (2005). Insolation-driven changes in atmospheric circulation over the past 116,000 years in subtropical Brazil. *Nature*, *434*(7029), 63–66. https://doi.org/10.1038/nature03365

Davies, R., Randall, D. A., & Corsetti, T. G. (1987). A fast radiation parameterization for atmospheric circulation models. *Journal of Geophysical Research*, *92*(D1), 1009–1016.

Decker, M., Brunke, M. A., Wang, Z., Sakaguchi, K., Zeng, X., & Bosilovich, M. G. (2012). Evaluation of the reanalysis products from GSFC, NCEP, and ECMWF using flux tower observations. *Journal of Climate*, *25*(6), 1916–1944. https://doi.org/10.1175/JCLI-D-11-00004.1

Dee, D., Uppala, S., Simmons, A., Berrisford, P., Poli, P., Kobayashi, S., et al. (2011). The ERA-interim reanalysis: Configuration and performance of the data assimilation system. *Quarterly Journal of the Royal Meteorological Society*, *137*(656), 553–597. https://doi.org/10.1002/qj.828

Doelling, D. R., Loeb, N. G., Keyes, D. F., Nordeen, M. L., Morstad, D., Nguyen, C., et al. (2013). Geostationary enhanced temporal interpolation for CERES flux products. *Journal of Atmospheric and Oceanic Technology*, *30*(6), 1072–1090. https://doi.org/10.1175/JTECH-D-12-00136.1

Gui, S., Liang, S., & Li, L. (2010). Evaluation of satellite-estimated surface longwave radiation using ground-based observations. *Journal of Geophysical Research*, *115*, D18214. https://doi.org/10.1029/2009JD013635

Gupta, S. K., Kratz, D. P., Stackhouse, P. W., Jr, A. C. W., Zhang, T., & Sothcott, V. E. (2010). Improvement of surface longwave flux algorithms used in CERES processing. *Journal of Applied Meteorology and Climatology*, *49*(7), 1579–1589. https://doi.org/10.1175/2010JAMC2463.1

Gupta, S. K., Ritchey, N. A., Wilber, A. C., Whitlock, C. H., Gibson, G. G., & Stackhouse Jr, P. W. (1999). A climatology of surface radiation budget derived from satellite data. *Journal of Climate*, *12*(8), 2691–2710. https://doi.org/10.1175/1520-0442(1999)012%3C2691:ACOSRB%3E2.0.CO;2

Harmel, R. D., & Smith, P. K. (2007). Consideration of measurement uncertainty in the evaluation of goodness-of-fit in hydrologic and water quality modeling. *Journal of Hydrology*, *337*(3-4), 326–336. https://doi.org/10.1016/j.jhydrol.2007.01.043

Hillis, D. M., & Bull, J. J. (1993). An empirical test of bootstrapping as a method for assessing confidence in phylogenetic analysis. *Systematic Biology*, *42*(2), 182–192. https://doi.org/10.1093/sysbio/42.2.182

Hinkelman, L. M., Jr, P. W. S., Wielicki, B. A., Zhang, T., & Wilson, S. R. (2009). Surface insolation trends from satellite and ground measurements: Comparisons and challenges. *Journal of Geophysical Research*, *114*, D00D20. https://doi.org/10.1029/2008JD011004

Jia, A., Jiang, B., Liang, S., Zhang, X., & Ma, H. (2016). Validation and spatiotemporal analysis of CERES surface net radiation product. *Remote Sensing*, *8*(12), 90. https://doi.org/10.3390/rs8020090

Jiang, B., Liang, S., Ma, H., Zhang, X., Xiao, Z., Zhao, X., et al. (2016). GLASS daytime all-wave net radiation product: Algorithm development and preliminary validation. *Remote Sensing*, *8*(3), 222. https://doi.org/10.3390/rs8030222

Jiang, B., Zhang, Y., Liang, S., Wohlfahrt, G., Arain, A., Cescatti, A., et al. (2015). Empirical estimation of daytime net radiation from shortwave radiation and ancillary information. *Agricultural & Forest Meteorology*, *211–212*, 23–36.

Jiang, B., Zhang, Y., Liang, S., Zhang, X., & Xiao, Z. (2014). Surface daytime net radiation estimation using artificial neural networks. *Remote Sensing*, *6*(12), 11,031–11,050. https://doi.org/10.3390/rs61111031

Jiménez-Muñoz, J. C., Sobrino, J. A., & Mattar, C. (2012). Recent trends in solar exergy and net radiation at global scale. *Ecological Modelling*, *228*, 59–65. https://doi.org/10.1016/j.ecolmodel.2011.12.027

Joseph, J. H., Wiscombe, W., & Weinman, J. (1976). The Delta-Eddington approximation for radiative flux transfer. *Journal of the Atmospheric Sciences*, *33*(12), 2452–2459. https://doi.org/10.1175/1520-0469(1976)033%3C2452:TDEAFR%3E2.0.CO;2

Kato, S., Loeb, N. G., Rose, F. G., Doelling, D. R., Rutan, D. A., Caldwell, T. E., et al. (2013). Surface irradiances consistent with CERES-derived top-of-atmosphere shortwave and longwave irradiances. *Journal of Climate*, *26*(9), 2719–2740. https://doi.org/10.1175/JCLI-D-12-00436.1

Kato, S., Loeb, N. G., Rutan, D. A., Rose, F. G., Sun-Mack, S., Miller, W. F., & Chen, Y. (2012). Uncertainty estimate of surface irradiances computed with MODIS-, CALIPSO-, and CloudSat-derived cloud and aerosol properties. *Surveys in Geophysics*, *33*(3-4), 395–412. https://doi.org/10.1007/s10712-012-9179-x

Kobayashi, S., Ota, Y., Harada, Y., Ebita, A., Moriya, M., Onoda, H., et al. (2015). The JRA-55 reanalysis: General specifications and basic characteristics. *Journal of the Meteorological Society of Japan Ser. II*, *93*(1), 5–48. https://doi.org/10.2151/jmsj.2015-001

Li, Z., Niu, F., Lee, K. H., Xin, J., Hao, W. M., Nordgren, B., et al. (2007). Validation and understanding of moderate resolution imaging Spectroradiometer aerosol products (C5) using ground-based measurements from the handheld Sun photometer network in China. *Journal of Geophysical Research*, *112*, D22S07. https://doi.org/10.1029/2007JD008479

Liang, S. (2004). *Quantitative remote sensing of land surfaces*. Hoboken, NJ: John Wiley. https://doi.org/10.1111/j.0031-868X.2004.295_1.x

Liang, S., Wang, K., Zhang, X., & Wild, M. (2010). Review on estimation of land surface radiation and energy budgets from ground measurement, remote sensing and model simulations. *IEEE Journal of Selected Topics in Applied Earth Observations and Remote Sensing*, *3*(3), 225–240. https://doi.org/10.1109/JSTARS.2010.2048556

Liang, S., Zhang, X., Xiao, Z., Cheng, J., Liu, Q., & Zhao, X. (2014). Global LAnd surface satellite (GLASS) products. *Springerbriefs in Earth Sciences*. https://doi.org/10.1007/978-3-319-02588-9

Liang, S., Zhao, X., Liu, S., Yuan, W., Cheng, X., Xiao, Z., et al. (2013). A long-term global LAnd surface satellite (GLASS) data-set for environmental studies. *International Journal of Digital Earth*, *6*, 5–33. https://doi.org/10.1080/17538947.2013.805262

Lin, B., Jr, P. W. S., Minnis, P., Wielicki, B. A., Hu, Y., Sun, W., et al. (2008). Assessment of global annual atmospheric energy balance from satellite observations. *Journal of Geophysical Research*, *113*, D16114. https://doi.org/10.1029/2008JD009869

Mercado, L. M., Bellouin, N., Sitch, S., Boucher, O., Huntingford, C., Wild, M., & Cox, P. M. (2009). Impact of changes in diffuse radiation on the global land carbon sink. *Nature*, *458*(7241), 1014–1017. https://doi.org/10.1038/nature07949

Minnis, P., Sun-Mack, S., Chen, Y., Khaiyer, M. M., Yi, Y., Ayers, J. K., et al. (2011). CERES edition-2 cloud property retrievals using TRMM VIRS and Terra and Aqua MODIS data—Part II: Examples of average results and comparisons with other data. *IEEE Transactions on Geoscience and Remote Sensing*, *49*(11), 4401–4430. https://doi.org/10.1109/TGRS.2011.2144602

Minnis, P., Sun-Mack, S., Young, D. F., Heck, P. W., Garber, D. P., Chen, Y., et al. (2011). CERES edition-2 cloud property retrievals using TRMM VIRS and Terra and Aqua MODIS data—Part I: Algorithms. *IEEE Transactions on Geoscience and Remote Sensing*, *49*(11), 4374–4400. https://doi.org/10.1109/TGRS.2011.2144601

Mlawer, E. J., Taubman, S. J., Brown, P. D., Iacono, M. J., & Clough, S. A. (1997). Radiative transfer for inhomogeneous atmospheres: RRTM, a validated correlated-k model for the longwave. *Journal of Geophysical Research*, *102*(D14), 16,663–16,682. https://doi.org/10.1029/97JD00237

Ou, S., Liou, K.-N., Gooch, W., & Takano, Y. (1993). Remote sensing of cirrus cloud parameters using advanced very-high-resolution radiometer 3.7-and 10.9-μm channels. *Applied Optics*, *32*(12), 2171–2180. https://doi.org/10.1364/AO.32.002171

Pan, X., Liu, Y., & Fan, X. (2015). Comparative assessment of satellite-retrieved surface net radiation: An examination on CERES and SRB datasets in China. *Remote Sensing*, *7*(12), 4899–4918. https://doi.org/10.3390/rs70404899

Peel, M. C., Finlayson, B. L., & Mcmahon, T. A. (2007). Updated world map of the Köppen-Geiger climate classification. *Hydrology and Earth System Sciences*, *4*(2), 439–473. https://doi.org/10.5194/hessd-4-439-2007

Ramanathan, V., Crutzen, P., Kiehl, J., & Rosenfeld, D. (2001). Aerosols, climate, and the hydrological cycle. *Science*, *294*(5549), 2119–2124. https://doi.org/10.1126/science.1064034

Rienecker, M. M., Suarez, M. J., Gelaro, R., Todling, R., Bacmeister, J., Liu, E., et al. (2011). MERRA: NASA's Modern-Era Retrospective analysis for Research and Applications. *Journal of Climate*, *24*(14), 3624–3648. https://doi.org/10.1175/JCLI-D-11-00015.1

Roesch, A., Wild, M., Ohmura, A., Dutton, E. G., Long, C. N., & Zhang, T. (2011). Corrigendum to "assessment of BSRN radiation records for the computation of monthly means" published in Atmos. Meas. Tech., 4, 339–354, 2011. *Atmospheric Measurement Techniques Discussions*, *4*(2), 975–1018.

Rose, F. G., Rutan, D. A., Charlock, T., Smith, G. L., & Kato, S. (2013). An algorithm for the constraining of radiative transfer calculations to CERES-observed broadband top-of-atmosphere irradiance. *Journal of Atmospheric and Oceanic Technology*, *30*(6), 1091–1106. https://doi.org/10.1175/JTECH-D-12-00058.1

Shi, Q., & Liang, S. (2013). Characterizing the surface radiation budget over the Tibetan Plateau with ground-measured, reanalysis, and remote sensing data sets: 1. Methodology. *Journal of Geophysical Research: Atmospheres*, *118*, 9642–9657. https://doi.org/10.1002/jgrd.50720

Sicart, J. E., Essery, R. L., Pomeroy, J. W., Hardy, J., Link, T., & Marks, D. (2004). A sensitivity study of daytime net radiation during snowmelt to forest canopy and atmospheric conditions. *Journal of Hydrometeorology*, *5*(5), 774–784. https://doi.org/10.1175/1525-7541(2004)005%3C0774:ASSODN%3E2.0.CO;2

Steffen, K., & Box, J. (2001). Surface climatology of the Greenland ice sheet: Greenland climate network 1995–1999. *Journal of Geophysical Research*, *106*(D24), 33,951–33,964. https://doi.org/10.1029/2001JD900161

Suarex, M. J., & Chou, M. D. (1994). *An efficient thermal infrared radiation parameterization for use in general circulation models*. Paper Presented at Global Modeling and Data Assimilation, Technical Memorandum 104606, Goddard Space Flight Center, Greenbelt, 102. https://doi.org/10.4236/ajcc.2015.41006

Trenberth, K. E., & Fasullo, J. T. (2010). Simulation of present-day and twenty-first-century energy budgets of the southern oceans. *Journal of Climate*, *23*(2), 440–454. https://doi.org/10.1175/2009JCLI3152.1

Troy, T. J., & Wood, E. F. (2009). Comparison and evaluation of gridded radiation products across northern Eurasia. *Environmental Research Letters*, *4*(4), 045008. https://doi.org/10.1088/1748-9326/4/4/045008

Verma, M., Fisher, J. B., Mallick, K., Ryu, Y., Kobayashi, H., Guillaume, A., et al. (2016). Global surface net-radiation at 5 km from MODIS Terra. *Remote Sensing*, *8*(12), 739. https://doi.org/10.3390/rs8090739

Walsh, J. E., Chapman, W. L., & Portis, D. H. (2009). Arctic cloud fraction and radiative fluxes in atmospheric reanalyses. *Journal of Climate*, *22*(9), 2316–2334. https://doi.org/10.1175/2008JCLI2213.1

Wang, K., & Dickinson, R. E. (2013). Global atmospheric downward longwave radiation at the surface from ground-based observations, satellite retrievals, and reanalyses. *Reviews of Geophysics*, *51*, 150–185. https://doi.org/10.1002/rog.20009

Wild, M. (2008). Short-wave and long-wave surface radiation budgets in GCMs: A review based on the IPCC-AR4/CMIP3 models. *Tellus A*, *60*(5), 932–945. https://doi.org/10.1111/j.1600-0870.2008.00342.x

Wild, M., Folini, D., Hakuba, M. Z., Schär, C., Seneviratne, S. I., Kato, S., et al. (2015). The energy balance over land and oceans: An assessment based on direct observations and CMIP5 climate models. *Climate Dynamics*, *44*(11-12), 3393–3429. https://doi.org/10.1007/s00382-014-2430-z

Wild, M., Folini, D., Schär, C., Loeb, N., Dutton, E. G., & König-Langlo, G. (2013). The global energy balance from a surface perspective. *Climate Dynamics*, *40*(11-12), 3107–3134. https://doi.org/10.1007/s00382-012-1569-8

Wild, M., Grieser, J., & Schär, C. (2008). Combined surface solar brightening and increasing greenhouse effect support recent intensification of the global land-based hydrological cycle. *Geophysical Research Letters*, *35*, L17706. https://doi.org/10.1029/2008GL034842

Wilson, K. B., Baldocchi, D. D., Aubinet, M., Berbigier, P., Bernhofer, C., Han, D., et al. (2002). Energy partitioning between latent and sensible heat flux during the warm season at FLUXNET sites. *Water Resources Research*, *38*(12), 1294. https://doi.org/10.1029/2001WR000989

Wu, F., & Fu, C. (2011). Assessment of GEWEX/SRB version 3.0 monthly global radiation dataset over China. *Meteorology and Atmospheric Physics*, *112*(3-4), 155–166. https://doi.org/10.1007/s00703-011-0136-x

Xia, X. A., Wang, P. C., Chen, H. B., & Liang, F. (2006). Analysis of downwelling surface solar radiation in China from National Centers for environmental prediction reanalysis, satellite estimates, and surface observations. *Journal of Geophysical Research*, *111*, D09103. https://doi.org/10.1029/2005JD006405

Yao, Y., Liang, S., Cheng, J., Liu, S., Fisher, J. B., Zhang, X., et al. (2013). MODIS-driven estimation of terrestrial latent heat flux in China based on a modified Priestley–Taylor algorithm. *Agricultural and Forest Meteorology*, *171*, 187–202.

Zhang, L., Dawes, W., & Walker, G. (2001). Response of mean annual evapotranspiration to vegetation changes at catchment scale. *Water Resources Research*, *37*(3), 701–708. https://doi.org/10.1029/2000WR900325

Zhang, X., Liang, S., Wang, G., Yao, Y., Jiang, B., & Cheng, J. (2016). Evaluation of the reanalysis surface incident shortwave radiation products from NCEP, ECMWF, GSFC, and JMA using satellite and surface observations. *Remote Sensing*, *8*(3), 225. https://doi.org/10.3390/rs8030225

Zhang, X., Liang, S., Wild, M., & Jiang, B. (2015). Analysis of surface incident shortwave radiation from four satellite products. *Remote Sensing of Environment*, *165*, 186–202. https://doi.org/10.1016/j.rse.2015.05.015